Contents lists available at ScienceDirect

International Journal of Rock Mechanics and Mining Sciences

journal homepage: http://ees.elsevier.com

Modelling gas flow in clay materials incorporating material heterogeneity and embedded fractures

I.P. Damians[a,b,*], S. Olivella[a,b], A. Gens[a,b]

[a] Department of Civil and Environmental Engineering (DECA), School of Civil Engineering, Universitat Politècnica de Catalunya – BarcelonaTech (UPC). UPC Campus Nord, Jordi Girona 1-3, Building D2, 08034 Barcelona, Spain
[b] International Centre for Numerical Methods in Engineering (CIMNE). UPC Campus Nord, Gran Capità s/n, Building C1, 08034 Barcelona, Spain

ARTICLE INFO

Keywords
Hydro-gas-mechanical 3D model
Gas flow
Embedded fracture model
Material heterogeneity

ABSTRACT

A series of gas injection tests on compacted bentonite were carried out at the British Geological Survey. Tests measurements included pressure and rate of gas inflow, gas outflow volume as well as stresses and pore pressure observed at various points of the sample. Tests were performed with two different gas injection systems: injecting the gas from one end of the sample (axial flow) or from one point at the centre of the sample (spherical flow). A coupled hydro-gas-mechanical 3D numerical model has been developed to simulate the tests. Initial permeability is assumed heterogeneous throughout the specimen and embedded fractures are incorporated in the formulation. Gas pressure-induced deformations during the test lead to variations of permeability due to changes in matrix porosity and, especially, fracture aperture. The model is able to reproduce satisfactorily the observed behaviour of the tests including the existence of preferential gas flow paths. A programme of sensitivity analyses involving the variation of different aspects and parameters of the model contributes to a better understanding of the phenomenon and highlights its complexity. The application of the same formulation and parameters calibrated in the axial flow test results in a successful simulation of the spherical flow test.

1. Introduction

1.1. General

The investigation of gas flow through clay materials is an active research area involving the development of new experimental techniques and new numerical approaches. Although there is still an incomplete understanding of the processes taking place, there are a number of relevant contributions in the literature, as mentioned below.

Harrington and Horseman[1] studied the gas transport properties of clay materials and **Marschall *et al.***[2] characterized argillaceous rocks regarding gas transport properties. Argillaceous rocks and clay based engineered materials (blocks and pellets) are candidate components for multi-barrier systems for isolation of different types of waste. In a different context, **Binning *et al.***[3] studied the transport of gases in the unsaturated zone related to oxidation process.

Arnedo *et al.*[4,5] presented modelling work for clay based materials using heterogeneous fields for the transport properties coupled to deformations. **Harrington *et al.***[6] studied the development of network induced by gas migration in pre-compacted bentonite. These works focus on the fact that gas migration takes place through preferential paths instead of being a uniform process of nonlinear diffusion. Regarding the localization of gas migration, **Wiseal *et al.***[7] did a study of visualization to understand the gas migration process in clay-rich materials.

Changes in the structure of the material and local deformations are important to explain gas movement. **Mahjoub *et al.***[8] developed a numerical study of the expansion of the argillite rock during gas injection. **Guo and Fall**[9] developed models for the dilatancy-controlled gas flow in bentonitic clays. Finally, **Zhu *et al.***[10] performed an experimental and numerical study for the gas transfer in shale rocks in the context of carbon sequestration.

In spite of all this work, there are still open questions regarding a number of gas-flow related features: entry-pressure, break-through-pressure, preferential/dilatant path formation and degree of desaturation of the material due to gas flow. Classical approaches for homogeneous porous media that consider retention curve as a nonlinear function of capillary pressure, and permeability as nonlinear function of saturation (or capillary pressure) are insufficient to provide a satisfactory representation of the phenomenon. It seems that material heterogeneity and local deformability play a major role and material properties do not remain constant during the gas flow process. The initial structure of the medium is not homogeneous and changes in structure and hydraulic properties can be caused by deformations. It is unclear whether changes in water content also play a role, but in principle gas migration

* Corresponding author.
E-mail addresses: ivan.puig@upc.edu (I.P. Damians); sebastia.olivella@upc.edu (S. Olivella); antonio.gens@upc.edu (A. Gens)

https://doi.org/10.1016/j.ijrmms.2020.104524
Received 13 April 2020; Received in revised form 7 October 2020; Accepted 15 October 2020
Available online xxx
1365-1609/

does not require significant desaturation to take place and hence it is uncertain whether swelling and contraction of clay aggregates are significant.

In this work, the general approach for multiphase flow modelling in deformable porous media is used together with additional features that have been with the objective to facilitate the formation of preferential paths for gas migration.

1.2. Gas flow through bentonite material: brief description of the performed tests

A series of tests (two of them described and modelled in this paper) were designed and performed in order to improve the understanding of the gas migration through clay-based materials in nuclear waste repositories. These tests were carried out at the British Geological Survey, and two of them constitute the dataset for Stage 1A and 2A of Task ENGINEER of the DECOVALEX-2019 international project[1,11,12]. Both axial and spherical gas injection tests were carried out on compacted Mx80.

A brief description of experiments is included herein for completeness. In the tests, gas pressure was increased until the entry pressure was exceeded and gas entered the sample. The gas then migrated through the clay and changes in pore-water pressure, swelling pressure and flowrate were observed by the instrumentation placed around the sample. When gas breakthrough occurred, gas outflow was recorded from the changes in pressure of the backpressure. The samples is enclosed in a rigid pressure vessel, so overall volume changes are negligible during the test. The experimental data shows that dynamic processes operate within the clay causing a variety of responses to be recorded on the monitoring instruments.

Fig. 1a shows a global view of the testing cell. More details of the testing apparatus including geometry and instrumentation of the Mx80 tests can be found in Daniels and Harrington.[12].

Two type of tests were carried out[1]: Axial gas flow test through saturated bentonite (test Mx80-D)[2] Spherical gas flow test through saturated bentonite (test Mx80-10). The names Axial and Spherical are used here to identify the tests. Axial means that the gas is injected on one side of the cylindrical sample, whereas Spherical means that the gas is injected in the centre of the cylindrical sample.

The Mx80-D test comprises two main stages: a hydration stage and a helium gas injection stage. The injection gas pressure was fixed at 1 MPa from 7.3 to 39.3 days and at 3 MPa from 39.4 to 46 days. Afterwards, the gas flow rate was continuously increased up to a constant flow rate value of 500 μL/h and then reduced to 375 μL/h until gas breakthrough was observed (at 71.5 days). After breakthrough and a period of gas flow through the sample, the injection pump was stopped whilst stresses and pore pressures were continuously monitored at several points on the sample up to the end of the test at day 121.

The Mx80-10 test consists in the injection at a point the centre of the cylindrical sample. A pressurization phase (water pressure increased progressively up to 6 MPa) takes place during the first 735 days. The injection process before 735 is not considered by the model in detail. Gas injection begins at day 735 at a constant flow rate of 125 μL/h. Flow rate increases to somewhat less than double and then decreases to one and a half times the initial value (this is detailed in the result comparison).

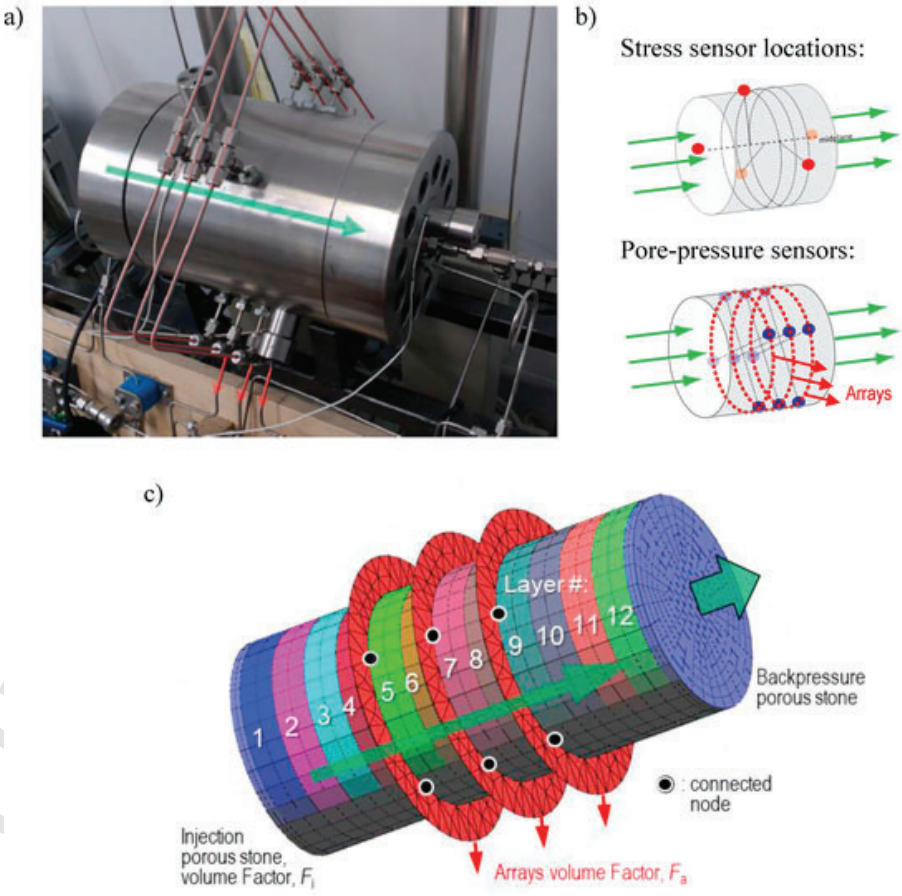

Fig. 1. (a) Radial sensor arrays detail (modified from **Daniels and Harrington[12]**), (b) stress and pore pressure radial sensor location schemes, and (c) 3D modelling representation of the sample by layers including arrays and injection/backpressure porous stone filters.

More information on the tests in the context of the modelling carried out in the project can be found in.[13].

2. Modelling approach

2.1. Conceptual model and background

A finite element method (FEM) three-dimensional (3D) model was developed to analyze the gas flow tests just described. The computer software CODE_BRIGHT was used to carry out the numerical simulations in this study. CODE_ BRIGHT[14,15] is a FEM simulation program developed at the Universitat Politècnica de Catalunya (DECA-UPC) and the International Centre for Numerical Methods in Engineering (CIMNE).

Preliminary calculations assuming porosity heterogeneity, which in turn produces heterogeneity of permeability and retention curve, were unable to provide a satisfactory description of the tests. This approach was unsuccessful because in the test, porosity changes were bound to be very small (it is a constant volume experiment) while the permeability changes required to model the flow and pressure gradients were expected to be quite large. Therefore, it was concluded that the initial assumption that the local material deformations produced changes in permeability and retention curve via porosity variations was not consistent with the real process and a different approach to model the variations of hydraulic properties was required.

As small discontinuities are likely to play a significant role in gas flow, an embedded discontinuity approach was introduced in the modelling.[16]. This approach permits differentiating between matrix and discontinuities intrinsic permeability. Discontinuities represent small micro-fractures or openings developing in the material leading to preferential flow paths. The concept is relatively simple and can be coupled to any mechanical constitutive equation. This approach is described in the next section.

Separate terms for matrix and fracture permeability (intrinsic and relative) were included in the modelling. The coupled hydro-gas-mechanical analysis has been performed postulating an initial heterogeneous distribution of permeability, initial embedded fractures aperture and spacing (defined in the next section) and the retention curve parameters. Porosity could be assumed initially uniform.

The balance equations solved are the conservation of water mass, conservation of helium mass and stress equilibrium. The primary variables were gas pressure and liquid pressure for the two-phase flow analysis. The mechanical equilibrium equations use displacements as primary variables. The conservation equations solved by CODE_BRIGHT can be found elsewhere[14,15].

Deformation was modelled assuming elasticity with net stress (fluid pressure as the maximum between gas and liquid). A dilatancy term was added to the standard elasticity equations. Permeability and retention curve were assumed to be a function of embedded fractures aperture and spacing. The detailed description of the model is presented in the following section.

2.2. Mechanical and hydraulic constitutive models

The mechanical model is based on elasticity with an additional term for dilatancy (ψ angle) included in the deviatoric component of the volumetric strains:

$$\begin{aligned}\Delta\varepsilon_{\mathrm{v}} &= \frac{\Delta p'}{K} - \frac{\Delta q}{3G}\tan\psi \\ \Delta\varepsilon_{d} &= \frac{\Delta q}{3G}\end{aligned} \tag{1}$$

where p' and q correspond to the net mean stress and deviatoric stress invariants, and K and G to the bulk and shear modulus, respectively (compression positive). Net mean stress is defined as total stress minus Biot's coefficient times fluid pressure (maximum between gas and liquid pressures), i.e., $p' = p - b\max\left(p_{\mathrm{g}}, p_{\mathrm{l}}\right)$ for positive compressions.

A constitutive model based on an integrated embedded permeability (**Olivella and Alonso**[16]) has been used for the modelling purposes of this study. The model is based on a decomposition of intrinsic permeability into matrix and discontinuities or fractures terms. Matrix and fracture intrinsic permeabilities undergo respective variation with porosity and aperture. Furthermore, in the present study, the intrinsic permeability decomposition is accompanied for the gas phase by a decomposition of the relative permeability. This is described by the equations below.

The global intrinsic permeability of the hydraulic model results from the combination of matrix and embedded fracture permeabilities according to the following equations:

$$\begin{aligned}k_{\mathrm{liquid}} &= k_{\mathrm{r,liquid}}\ \left(k_{\mathrm{matrix}} + k_{\mathrm{fractures}}\right) \\ k_{\mathrm{gas}} &= k_{\mathrm{r,gas\_matrix}}\ k_{\mathrm{matrix}} + k_{\mathrm{r,gas\_fractures}}\ k_{\mathrm{fractures}}\end{aligned} \tag{2}$$

where the relative permeability is a function of the effective degree of saturation ($S_{\mathrm{effective}}$), as:

$$\begin{aligned}k_{\mathrm{r,liquid}} &= \left(S_{\mathrm{l\_effective}}\right)^{n_{\mathrm{l}}} \\ k_{\mathrm{r,gas\_matrix}} &= \left(S_{\mathrm{g\_effective}}\right)^{n_{\mathrm{g\_matrix}}} \\ k_{\mathrm{r,gas\_fractures}} &= \left(S_{\mathrm{g\_effective}}\right)^{n_{\mathrm{g,fractures}}}\end{aligned} \tag{3}$$

The effective saturation is defined using a maximum and minimum degree of saturation, i.e., $S_{\mathrm{effective}} = \left(S - S_{\mathrm{min}}\right) / \left(S_{\mathrm{max}} - S_{\mathrm{min}}\right)$.

Incorporating both Eq. (3) into Eq. (2), results as:

$$\begin{aligned}k_{\mathrm{liquid}} &= \left(S_{\mathrm{l\_effective}}\right)^{n_{\mathrm{l}}}\left(k_{\mathrm{matrix}} + k_{\mathrm{fractures}}\right) \\ k_{\mathrm{gas}} &= \left(S_{\mathrm{g\_effective}}\right)^{n_{\mathrm{g\_matrix}}} k_{\mathrm{matrix}} + \left(S_{\mathrm{g\_effective}}\right)^{n_{\mathrm{g\_fractures}}} k_{\mathrm{fractures}}\end{aligned} \tag{4}$$

It should be noted that for gas flow, the decomposition into matrix and fracture terms is done for both intrinsic permeability and relative permeability. This was not considered necessary for the liquid flow.

The matrix permeability component is computed as:

$$k_{\mathrm{matrix}} = \frac{k_0\left(1-\varphi_0\right)^2}{\varphi_0^3}\frac{\varphi^3}{(1-\varphi)^2} \tag{5}$$

and the intrinsic permeability of the fracture is controlled, assuming laminar flow, by the aperture of the internal fractures (b), as:

$$k_{\mathrm{fracture}} = \frac{b^2}{12} \tag{6}$$

The equivalent fracture permeability results as:

$$k_{\mathrm{eq\_fractures}} = k_{\mathrm{fracture}}\frac{b}{a} = \frac{b^3}{12a} \tag{7}$$

where a refers to associated width for each embedded fracture, and the fracture aperture b depends on the strain level according to:

$$b = b_0 + \langle \varepsilon - \varepsilon_0 \rangle\, a \le b_{\mathrm{max}} \tag{8}$$

where ε and ε_0 refer to current and initial strains, respectively (with $\varepsilon > 0$ meaning extension), and the fractures width b_0 and b_{max} are defined in the equations for the material properties presented below. The mechanical behaviour is coupled to the hydraulic/gas because the volu-

metric strains cause changes in permeability, through changes in aperture.

The retention curve is defined by the following equation:

$$\frac{S_l - S_{l,min}}{S_{l,max} - S_{l,min}} = \left(1 + \left(\frac{(P_g - P_l) - P_{00}}{P_{VG}}\right)^{\frac{1}{1-\lambda_{VG}}}\right)^{-\lambda_{VG}} \quad (9)$$

where P_g, P_l are the gas and liquid pressures according to Van Genuchten model[17]; λ_{VG} is the shape function; and P_{VG} and P_{00} are the capillary pressure Van Genuchten parameters (where P_{00} corresponds to a finite air entry value; Eq. (9) valid for $(P_g - P_l) - P_{00} \geq 0$). P_{VG} is calculated as:

$$P_{VG} = P_0 \sqrt[3]{\frac{k_0}{k}} \quad (10)$$

where P_0 is the initial capillary pressure and k_0 is the initial permeability. It should be noted that the retention curve may change with the opening of fractures as pore size controls the gas entry values, and fractures may represent large pores leading to a reduction of gas entry value. Eq. (10) incorporates the cubic dependence of permeability with fracture aperture b and the capillary pressure dependence on fracture aperture, b, based on the equation for surface tension ($P_g - P_l = \sigma/b$, where σ is surface tension).

2.3. Model geometry and material heterogeneity

The 3D geometry of the sample was reproduced in the model (Fig. 1c). The domain was divided into small sub-zones to which different initial properties could be assigned. Model dimensions for the cylindrical sample test were, according to the specifications, 120 mm in length and 60 mm diameter. In addition, 5 mm-thick filters were included at each end of the sample (corresponding to injection and backpressure zones). A volume factor was internally incorporated to take into account the effective volume of the injection system (i.e., vessel, pipework, etc.). The experiment also contains arrays used for hydration and to perform radial measurements of pressure (Fig. 1a). Since these arrays were connected by pipelines, an additional volume represented by a ring surface (with a certain thickness) was considered. Both injection (i.e., porous stone filter) and array volume factors (F_i and F_a) are defined to ensure that the real volume in the apparatus is equal to F-times the volume in the model.

The numerical domain was discretized with a mesh of 7168 hexahedral elements and 8205 nodes. 375 triangular elements with a thickness of 1 mm were used to represent the volume associated to the arrays (see arrays detail in Fig. 1c).

2.4. Boundary and initial conditions

The pattern of gas flow though saturated clay specimens suggests that material heterogeneity plays a key role in the phenomenon. Consequently, an initially heterogeneous specimen was generated for the analyses. As mentioned above, sample heterogeneity based on variations of porosity was unable to provide an adequate representation of test observations. Instead heterogeneity was based on variations of permeability.

A layer-by-layer random permeability distribution was assumed, as shown in Fig. 2. Threw permeability values were considered. Fig. 2a shows the permeability distribution assuming that the three values have the same probability whereas the distribution shown in Fig. 2b is generated assuming that the lowest permeability has a probability of 2/3 and the other two permeabilities have a probability of 1/6. For simplicity, porosity can be considered constant as the predictive capability of the model is not affected.

As it is explained later in the sensitivity analysis section, in addition to this layer-by-layer random permeability distribution, also another case with a sort of connected permeability field (but still based on random permeability distribution) was generated (see Fig. 2c) aiming to produce preferential gas paths.

The sample is initially saturated with constant pore pressure of 0.1 MPa. An initial stress of 2 MPa was assumed, corresponding to the swelling stress reached by the material during saturation.

The volume factor (F_i) applied to the filter volume allows considering the actual injection volume present in the test that includes not only the porous stone, but also the interface vessel, pipework and any other additional device located in the gas injection before entering the bentonite sample. An injection volume of about 130 cm^3 was considered for the Base case (equivalent to $F_i = 15$ in the model). However, the effect of this parameter is later assessed as part of the programme of sensitivity analysis. The volume factor (F_a) to take into account the actual volume of the array system (2.2 cm^3) turned out to be 1, for the Base case, i.e., the actual volume in the experiment was equal to the volume of the array ring in the model (see Fig. 1c).

3. Axial gas flow: base case

3.1. Material properties and particular model features

The three sets of parameters to define the different hydraulic properties on the Base case (Case 1a) are presented in Table 1. The case includes material heterogeneity using the set of probabilities of 1/6, 1/6 and 2/3. The resulting variation of intrinsic permeability as a function of the deformation of the internal fracture spacing is presented in Fig. 3a. The same figure also shows the variation of the equivalent intrinsic permeability, defined by a weighted geometrical mean of the three values of permeability. It can be observed that the initial equivalent intrinsic permeability (3.3×10^{-21} m^2) is consistent with the value specified by Tamayo-Mas et al.[18] It can also be noted that the upper bound of the equivalent intrinsic permeability is 7.0×10^{-17} m^2.

Fig. 3b shows the relative permeability functions. The gas relative permeability function can be modified by changing the maximum gas saturation to calculate effective gas saturation in Eq. (3). A value of 0.3 for the maximum gas saturation produces a rapid increase of gas relative permeability as desaturation progresses. So the gas relative permeability function changes from 0 to 1 in the range of 0–0.3 for gas degree of saturation. To check the effect of this parameter, a sensitivity study to the value of the maximum gas saturation has been carried out and is presented below.

The soil material stiffness was defined by an Elastic modulus $E = 307$ MPa, and Poisson's ratio $\nu = 0.40$ corresponding to a shear modulus $G = 108.9$ MPa and bulk modulus $K = 568.5$ MPa. Values of $\psi = 24^\circ$ for dilatancy (see Eq. (1)) and 0.5 for Biot's coefficient were adopted (see Table 1).

In correspondence to the actual test, the gas flow rate (q_g) was prescribe. It increases linearly from 0 to 8.0×10^{-7} kg/s/m^2 (from 46 to 67 days) and is kept constant at 8.0×10^{-7} kg/s/m^2 afterwards (from 67 to 71.5 days).

As explained above, a layer-by-layer randomly permeability distribution with different weighting was considered in the model, resulting in three different model zones distinction. Base case was generated by a (2/3)-weighting distribution for the highest permeability value, and (1/6)-weighting distribution for the lower permeability values (see Fig. 2b).

This Base case (case 1a) corresponds to the analysis that best fit the experimental measured data. The Base case was reached after performing a comprehensive set of sensitivity analyses involving multiple cal-

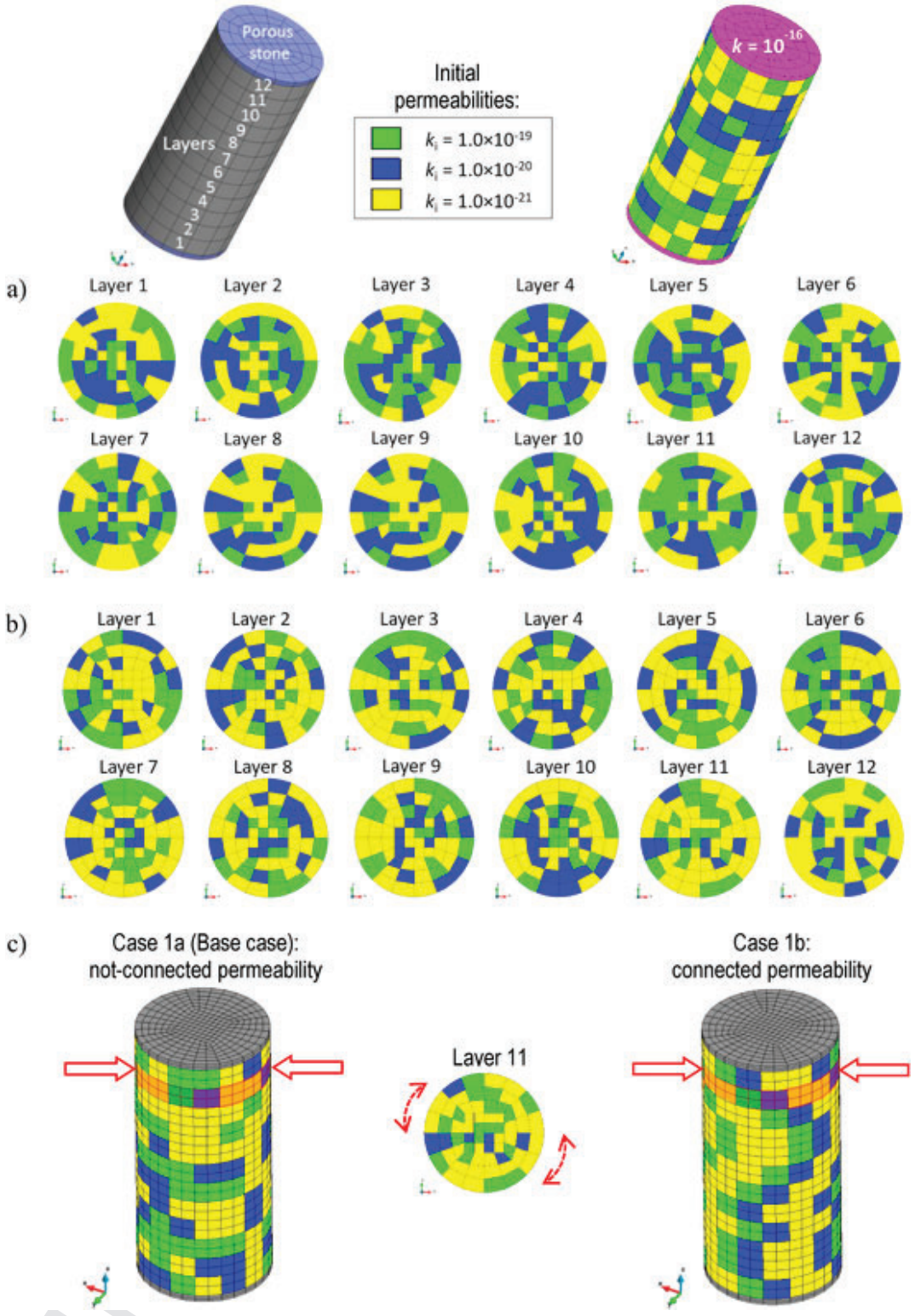

Fig. 2. Layer-by-layer random permeability distribution assumed for the not-connected case: (a) 1/3–1/3–1/3 weighting (see global distribution on top-right), (b) 1/6 (to $k_i = 1.0 \times 10^{-19}$ m^2) – 1/6 (to $k_i = 1.0 \times 10^{-20}$ m^2) – 2/3 (to $k_i = 1.0 \times 10^{-21}$ m^2) weighting, and (c) comparison between base case with not-connected random permeability (left) and connected initial permeability (right) (Note: connected case is generated from not-connected case 1/6-1/6-2/3 distribution Layer 11th with a layer-by-layer random rotation generation).

Table 1
Material model properties for the Base case.

Homogeneous part (same parameter value for the entire sample modelled):	
Mechanical parameters (Elasticity):	Values:
- Young's modulus, E:	307
- Poisson's ratio, ν:	0.4
- Dilatancy angle (elastic), ψ:	24
- Biot's coefficient:	0.5
Hydraulic parameters:	
Fick's law:	
- Tortuosity for dissolved gas:	0.5
- Dispersivity for dissolved gas:	0.01-axial and 0.001-radial
Relative permeability (Darcy's law):	
- Liquid, n_l,matrix$_{\&fractures}$:	3
- Max./min. liquid saturation, Sl:	1.0/0.0
- Gas, ng,matrix:	2
- Gas, ng,fractures:	1
- Max./min. gas saturation, Sg:	0.3/0.0
Other parameters:	
- Initial porosity, φ0:	0.44
- Dry density, ρdry:	1512
- Molar mass of Helium, M:	0.004
- Henry's constant, H:	10,000
Heterogeneous part (three different sample zones randomly distributed):	
Hydraulic parameters:	Values:
Water retention curve (van Genuchten):	
- Capillary pressure: P_0:	10.8//22.5//48.6
P_{00}:	1.2//2.5//5.4
- Shape function, λVG:	0.45
- Max./min. liquid saturation, Sl:	1.0/0.0
Intrinsic permeability (Darcy's law):	
Matrix:	
- Reference permeability, k_0:	1.0×10^{-19}//1.0×10^{-20}//1.0×10^{-21}
Fractures:	
- Associated width, a:	5.0×10^{-4}//5.0×10^{-5}//5.0×10^{-6}

Homogeneous part (same parameter value for the entire sample modelled):		
Mechanical parameters (Elasticity):		Values:
- Aperture:	initial, b_0:	9.5×10^{-9}//5.0×10^{-9}//1.5×10^{-9}
	maximum, b_{max}:	7.5×10^{-7}//3.5×10^{-7}//1.5×10^{-7}
- Initial strain, ε_0:		0.01//0.03//0.05

culations. The main sensitivity analyses carried out are described in the next section.

3.2. Model results and comparison with test observations

The comparisons between the Base case results and the measurements are presented in Fig. 4. They include the evolutions in time of gas volume inflow, gas volume outflow, injection pressure and backpressure, gas and liquid pressure measured in the arrays and radial and axial stresses. It can be observed that the calculated results yield a satisfactory agreement with the measured pore pressure data. In addition, the breakthrough point was well captured at about 60 days after gas injection, as well as the magnitude of the maximum gas pressure reached. It can also be noted that the measured pore pressure exhibits an irregular variation during gas dissipation at 70–80 days after the start of gas

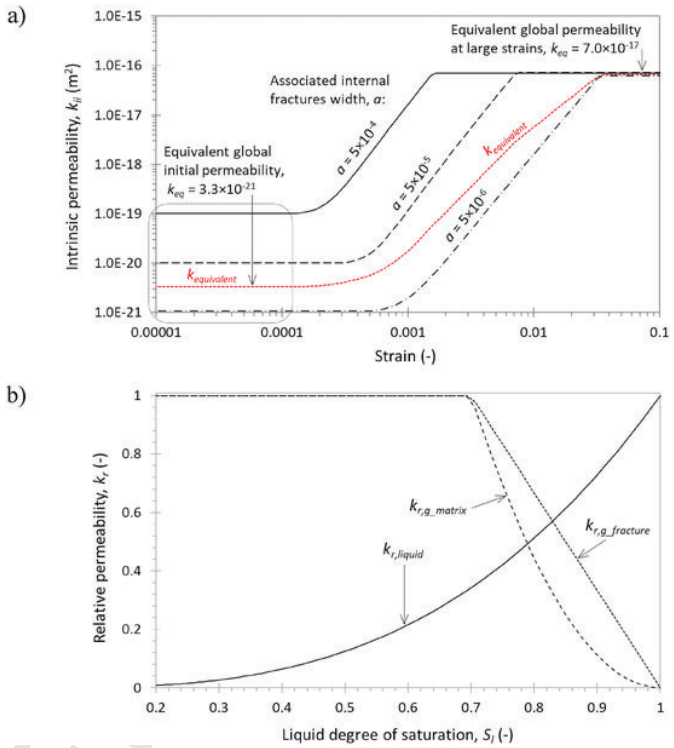

Fig. 3. (a) Intrinsic permeability evolution as a function of strain for Base case, and (b) relative permeability as a function of liquid saturation (Note: equivalent global permeability representation calculated by weighted geometric mean).

injection. The calculated liquid pressure results have also been plotted in order to show the same behaviour (see Fig. 4d).

The individual components of the computed helium mass flux at the mid cross section of the sample are plotted in Fig. 5. It can be observed, that a complex flux combination takes place: gas flow is controlled by diffusion of Helium in water from 10 to 40 days after gas injection, a combination of diffusion/dispersion and liquid flux advection from 40 to 65 days, and finally, a gas flux controlled by gas advective flux from 65 to 121 days. After breakthrough (determined at about 55 days in this mid-plane location), gas advection plays the dominant flux role while liquid flux decays and some diffusion/dispersion component remains. The computed maximum volumetric strains were about 0.3% compression at the back of the sample, whereas about 0.02% internal dilation strain was computed within the main body of the sample during gas breakthrough. Figures displaying the volumetric strains of the Base case before and during gas injection, as well as during gas dissipation, can be found in the Supplemental Material (Fig. S1).

Fig. 6 presents a sequential gas advection flux evolution within the model sample; the same scale range (1.0×10^{-8} kg/m^2/s to 1.0×10^{-7} kg/m^2/s) applies to all times. In order to better identify preferential gas flux paths, advective gas flux vectors are also plotted at a longitudinal cross-section of the model sample. As expected, gas flux goes through the higher permeability zones, generating preferential gas paths in the axial direction of the sample.

4. Sensitivity analysys of axial gas flow

4.1. General

A programme of sensitivity analyses has been carried out to provide a better understanding of the gas glow phenomenon as well as to determine the effects of a number of features of the numerical model developed.

The sensitivity analyses performed are listed in Tables 2 and 3. The parameters in boldface indicate that they are the same as in the

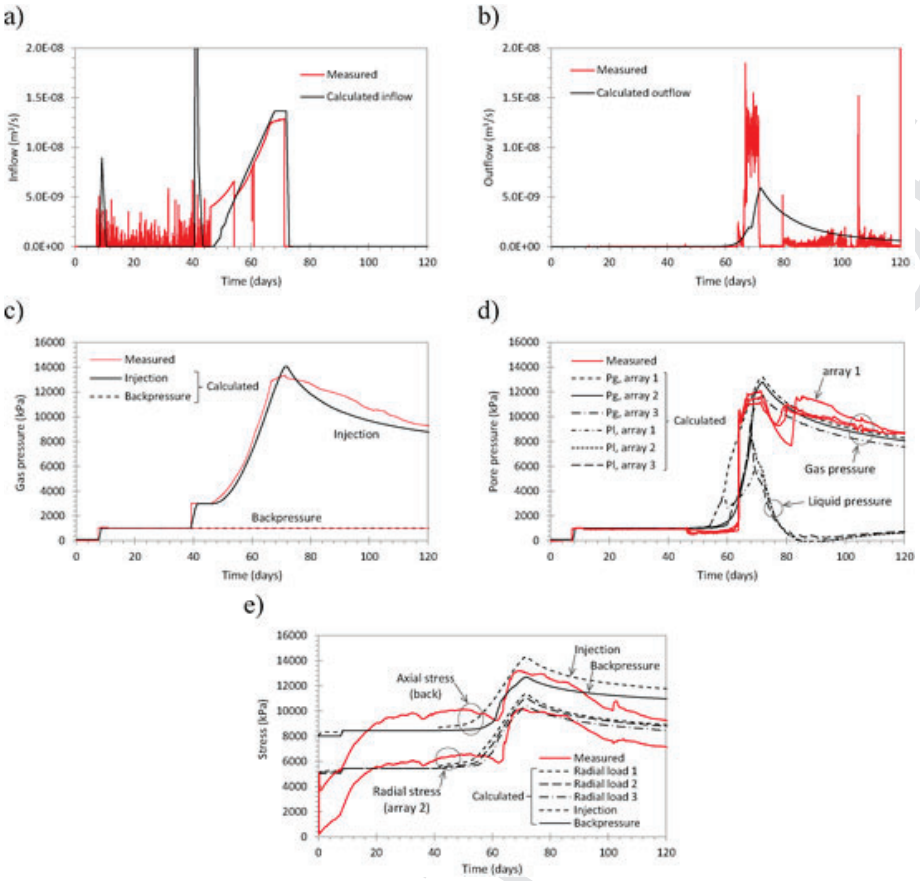

Fig. 4. Measured and calculated results from Base case (i.e., Case 1a): (a) injection flow, (b) outflow, (c) injection and backpressures, (d) gas – liquid pressure at arrays, and (e) radial – axial stresses.

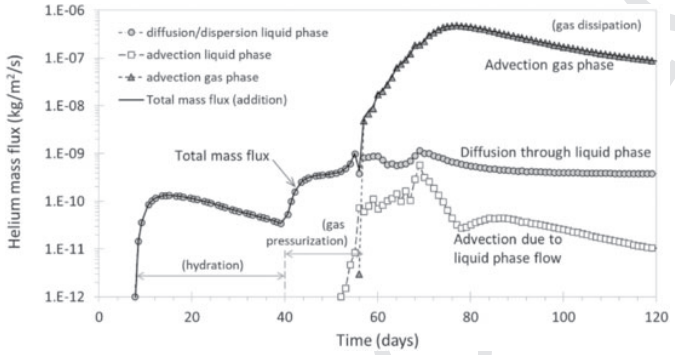

Fig. 5. Mass flux contributions at mid-plane of the model sample (Base Case 1a).

Base case. It can be noted that, for each particular sensitivity analysis, only one parameter is varied with respect to the Base case. Table 2 addresses the effects of material heterogeneity and connected permeability. Table 3 includes the analyses designed to examine the effect of changes in constitutive variables and boundary conditions. The following aspects are considered: material compressibility (Case 4), the initial permeability approximation at sub-zones (cases 5a and 5b), the maximum gas saturation assumption (cases 6a and 6b), external volumes of the testing system devices (cases 7a and 7b regarding the gas injection system and cases 8a and 8b the connected radial array sensors).

In the following sections all sensitivity cases are presented. The results of the new analyses are compared to experimental observations and to the results of the Base case. The following variables are compared: gas volume inflow, gas volume outflow, pore pressure at the injection point and in array 2, and mid-plane axial and radial stresses. Only the calculations in the observations of the representative array 2 are presented for simplicity.

However, in order to first show the range of response from all model cases, Fig. 7 presents together the injection gas pressure and gas outflow for all the sensitivity analyses. A significant range of results was obtained, with significant different responses in terms of their magnitude, variation pattern and time-dependent responses. As shown in the next sub-sections, in some cases, a better agreement with a particular measured data is associated with larger departures for other observations.

4.2. Gas injection strategy: gas pressure or gas flow rate prescribed

Two alternative strategies of gas injection test were performed:

- Gas pressure (P_g) prescribed according to the measured gas pressure (from 46 to 71.5 days).
- Gas flow rate (q_g) prescribed linearly increasing from 0 to 8.0×10^{-7} kg/s/m^2 (from 46 to 67 days) and kept constant at 8.0×10^{-7} kg/s/m^2 (from 67 to 71.5 days).

The prescribed gas flow rate (q_g) corresponds in fact to the real conditions in the test, where the gas pressure is a result of the applied flow rate and it is, therefore, a measured variable. The strategy of prescribed P_g was, however, initially useful to calibrate other model parameters. The numerical solution of the two options should converge to the same outcome when the parameters are correctly calibrated.

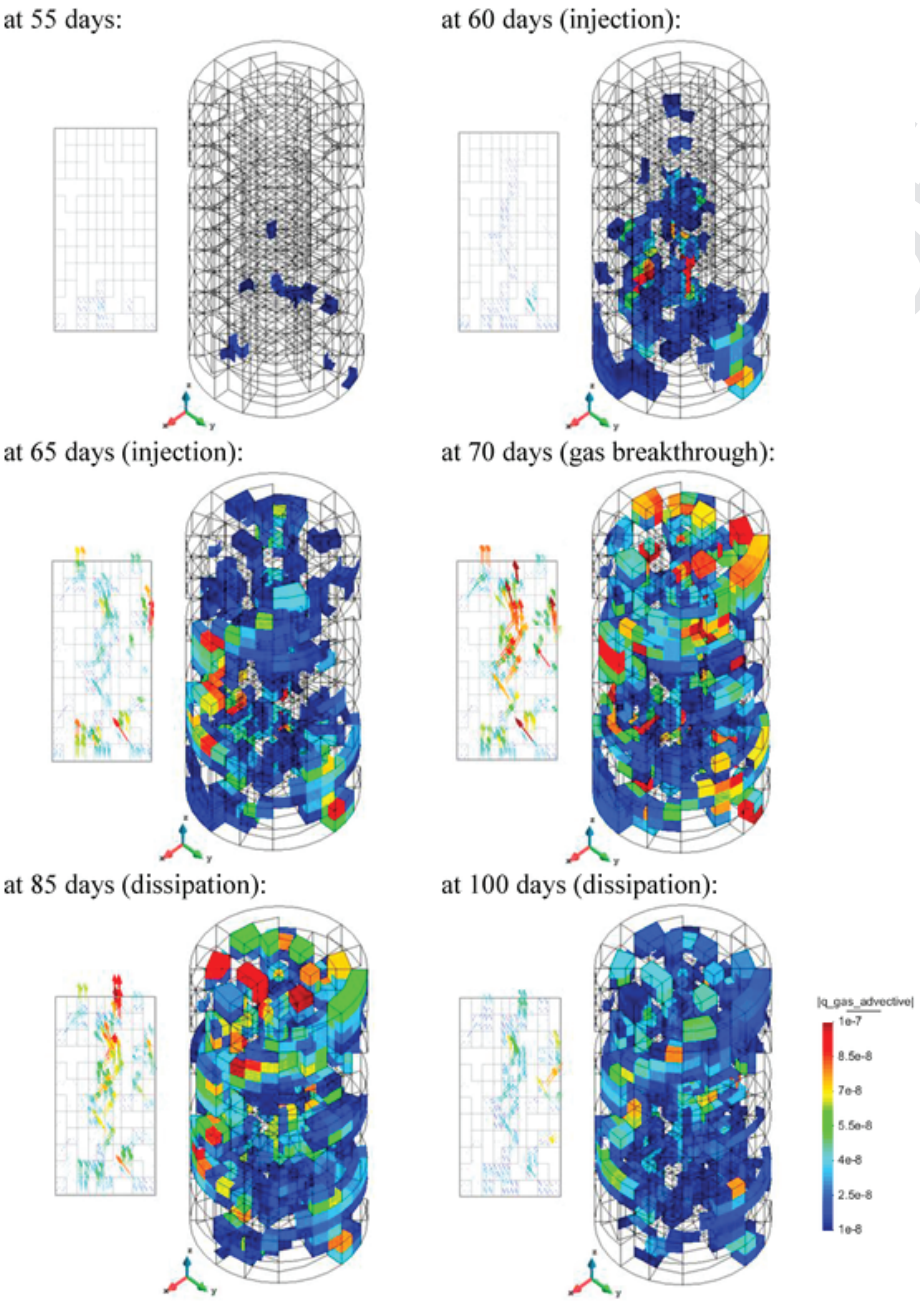

Fig. 6. Gas advection (m/s) distribution at different times during gas migration (Base Case 1a).

Fig. 8 presents the results from the two different gas injection strategies considered. As indicated above, the prescribed gas flow rate (q_g), used in Base case (Case 1a), and it is the one that corresponds to the real test conditions. Naturally, inflow results agree better with the prescribed q_g rather than with P_g (see Fig. 8a), and injection pressure was obviously better captured when P_g was prescribed (see Fig. 8c). Both q_g and P_g gas injection strategies returned similar response for the axial and radial stress results, where the stress variation was reasonably well captured (about 5.5 MPa in both models compared with about 4.5 MPa was determined in the test). The sudden stress increase was, however, not captured, in the same abrupt manner as in the model. Also, the stress decay variation was also obtained by both model cases, but not with the same slope. Furthermore, the comparison of outflow results shown in previous Fig. 7b demonstrates the difficulty to capture the measured response in spite of other results agreeing reasonably well with test observations.

4.3. Connected permeability, weighting distribution, and heterogeneity

In the Base case (Case 1a) the permeability was randomly distributed in the model (Fig. 4b) whereas in Case 1b a connected permeability field was generated by connecting high initial permeability sub-zones along the axial direction of the sample (Fig. 4c). In this way, gas flow through specific/preferential pathways was favoured. Both connected and not-connected permeability cases were generated through the random distribution of permeability values in the model discretization with the same weighting assumption (1/6–1/6–2/3). It must be noted that the global equivalent permeabilities (weighted geometric mean, calculated as the product of $k_a^{1/6}\, k_b^{1/6}\, k_c^{2/3}$) are the same in Cases

Table 2
List of cases to analyse the effect of material heterogeneity and connected permeability from Case 1a (Base case).

#	Heterogeneity Homogeneity	k-weighting distribution	Connectivity	$k_{eq,0}$ (m^2)	Comments:
1a	**heterogeneity**	**1/6-1/6-2/3**	**not-connected**	**3.3×10^{-21}**	**Base case**
1b			connected	3.3×10^{-21}	preferential path
2a		1/3-1/3-1/3	not-connected	1.0×10^{-20}	resulting from the k distribution change
2b				3.3×10^{-21}	prescribed (changing k_0 and geometric parameters from embedded fractures)
3a	homogenized		NA	3.3×10^{-21}	$k = k_{eq(1a)}$
3b				3.3×10^{-20}	$k = 10 \times k_{eq(1a)}$
3c				3.3×10^{-19}	$k = 100 \times k_{eq(1a)}$
3d				3.3×10^{-18}	$k = 1000 \times k_{eq(1a)}$

Table 3
List of cases to analyse the effect of different constitutive and/or boundary conditions from Case 1a (Base case).

#	Stiffness, E (MPa)	Initial permeability, k_i ($=C \times 10^{-19,-20,-21}$)	Maximum gas saturation Sg, max (%)	External system volumes:		Gas matrix n-power variable:
				Injection, Fi	Arrays, Fa	ng,matrix
1a	**307**	***C* = 1.0**	**30**	**15**	**1.0**	**2**
4	∞					
5a	**307**	$C = 0.5$ ($k_{eq} = 1.7 \times 10^{-21}$)				
5b		$C = 2.0$ ($k_{eq} = 6.5 \times 10^{-21}$)				
6a		***C* = 1.0**	50			
6b			5			
7a			**30**	25		
7b				5		
8a				**15**	0.05	
8b					5.0	
9a					**1.0**	1
9b						3

1a and 1b (i.e., $k_{eq} = 3.3 \times 10^{-21}$). Fig. 9 presents the relevant comparisons of the two cases. It can be noted that a significantly better outflow prediction was achieved with the connected permeability Case 1b (Fig. 9b). However, the assumption of this case more arbitrary than that of the Base case, as Case 1b forces the gas to flow through the higher permeability paths that are explicitly generated. The injection and array 2 gas pressures resulted in better response for the Case 1a, fitting more closely the decay variation of the measured data. Both cases resulted in a similar response concerning the measured development of stresses.

Fig. 10 shows the computed advective gas flux vectors and permeability at day 96 from the beginning of the test (i.e., during the gas dissipation stage). These results provide qualitative information about the gas flux through the sample. It can be observed that flux vectors show more direction variation in the not-connected case (Case 1a) compared to the connected one (Case 1b), where the flux is mostly oriented in the axial direction, due to the presence of preferential gas flow paths. Also, higher permeability paths are obtained associated with the preferential gas paths.

To examine the effect of different heterogenous distributions of permeability, cases 2a and 2b were performed assuming the same probability (1/3) for the three values of permeability. The difference between Case 2a and Case 2b is the resulting equivalent permeability value and its evolution with strains development (see dashed curves in Fig. 11a and b). The change of the weighting distribution produces a modification of the equivalent permeability in Case 2a. In Case 2b, the initial permeability values as well as the geometric parameters from the embedded fractures model (basically, the a-parameter, which relates to the associated width of the fractures; see Eqs. (7) and (8) are modified to obtain the same equivalent permeability variation with changing strain as in the Base case. The effect of this different weighting permeability distribution is shown in Fig. 12. The change to a uniform 1/3-weighting in Case 2a reduces gas pressure evolution both at the injection point and in the arrays (see Fig. 12a and c), and it also increases the outflow magnitude (Fig. 12b). It should be noted, however, that Case 2a involves a higher global-equivalent permeability of the material up to on order of magnitude: $k_{eq(2a)} = 1.0 \times 10^{-20}$ m^2 $\gg k_{eq(1a)} = 3.3 \times 10^{-21}$ m^2 (see Fig. 11a).

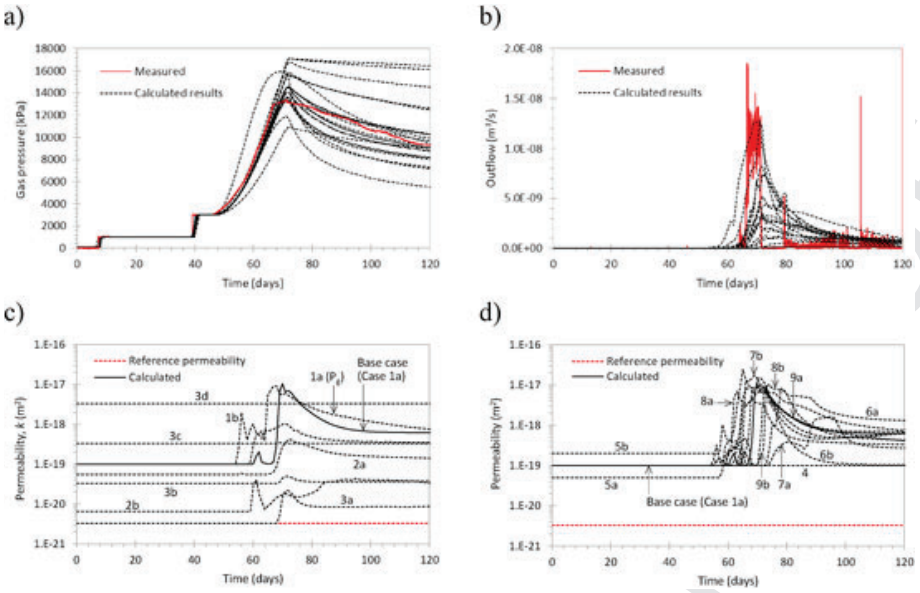

Fig. 7. Summary of all sensitivity cases compared with measured data (red curve): (a) injection pressure, (b) outflow, and (c,d) maximum permeability variations at the middle of the sample for cases presented in Tables 2 and 3, respectively. (For interpretation of the references to colour in this figure legend, the reader is referred to the Web version of this article.)

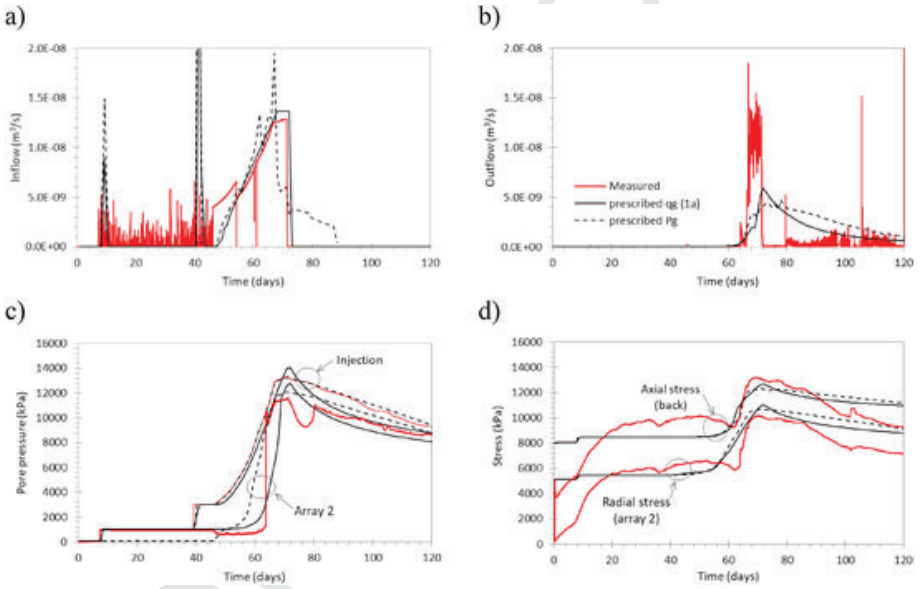

Fig. 8. Comparison between gas injection strategies, i.e., prescribed P_g or q_g: (a) injection pressure, (b) outflow, (c) pore-pressure at array 2, and (d) axial and radial stresses.

Case 2b also uses the uniform 1/3-weighting but with small changes to the geometrical parameter values defining the embedded fractures (i.e., *a* and *b* parameters; see Fig. 2) in order to achieve the same equivalent permeability (i.e., $k_{eq(2b)} = k_{eq(1a)}$; see Fig. 11b). This change, however, does not results in a better performance of the model in any of the compared results: a much higher injection gas pressure, a clear delay of the pressure obtained at array 2, a much lower outflow and less decay variation of the stress evolution after breakthrough are obtained.

To explore further the role of heterogeneity, a number of analyses of homogenous specimens have been performed (cases 3a to 3d). Cases 3a to 3d refer to homogenous material models, all the domain has the same permeability. The differences between the various cases is the permeability value: 3.3×10^{-21} m^2 for the Case 3a (corresponding the k_{eq}-value of Case 1a as well as to the value from test specifications) and 3.3×10^{-20} m^2, 3.3×10^{-19} m^2 and 3.3×10^{-18} m^2 for cases 3b, 3c and 3d, respectively. It should be noted that these higher permeability values are not realistic for the Mx80 material or other bentonites. The different permeability evolutions with regards to strain development are shown in Fig. 11c.

Fig. 13 presents comparison results doe the cases involving homogenous samples. It can be observed that a good approximation of gas pressure to the measured and Base case results requires a much higher permeability for a bentonite. Furthermore, even with a very high permeability value of 3.30×10^{-18} m^2 (Case 3d), the gas outflow was lower than in the Base case. All the other homogenous analyses with lower permeabilities do not show any significant outflow response. Thus, it is not possible to obtain satisfactory results even when using unrealistically high value of bentonite permeability.

4.4. Material compressibility, permeability, and maximum gas saturation

The effect of assuming an incompressible material (Case 4) is shown in Fig. 14a; a different response from the Base case is obtained. Whereas the breakthrough time-point is better captured at array 2, the

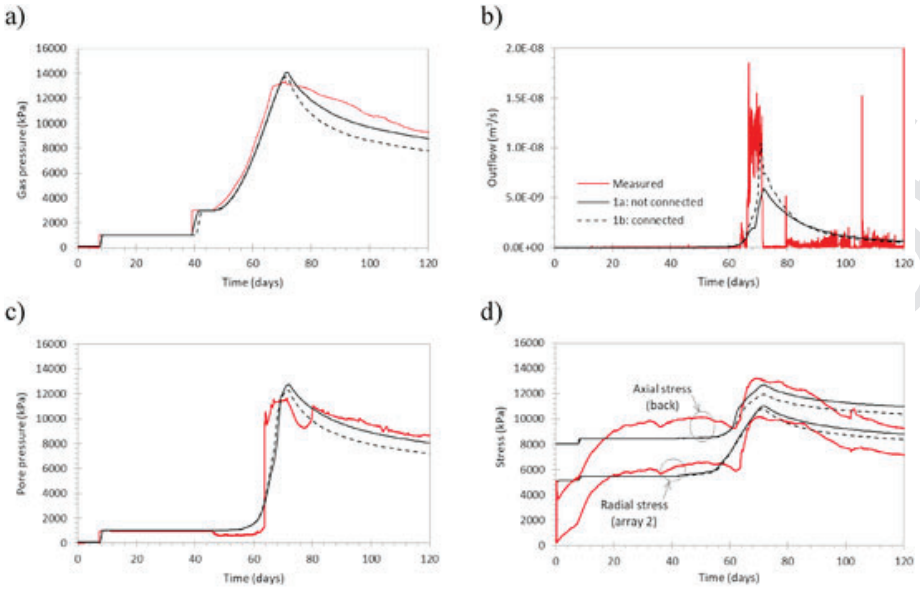

Fig. 9. Comparison between not-connected and connected permeability cases: (a) injection pressure, (b) outflow, (c) pore-pressure at array 2, and (d) axial and radial stresses (Cases 1).

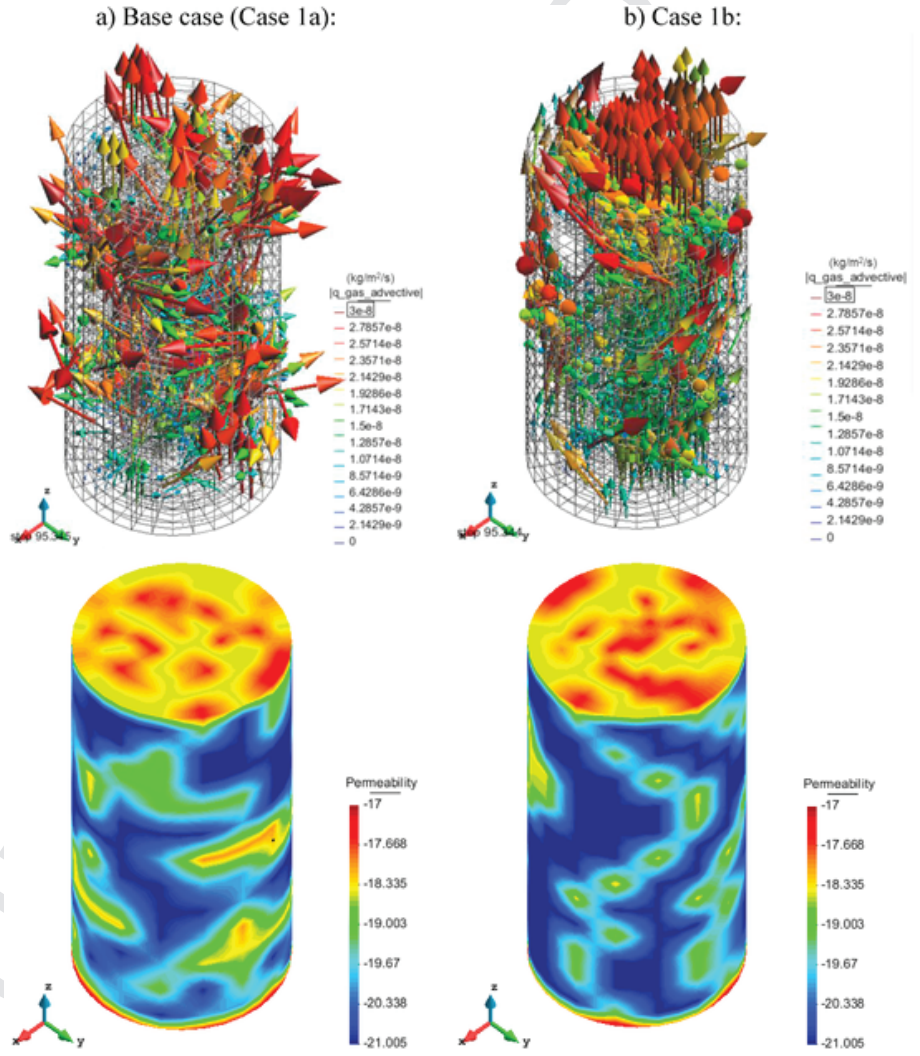

Fig. 10. Comparison between advective gas flux vectors and permeability at 95 days (during gas dissipation) for (a) not-connected and (b) connected permeability cases (Cases 1).

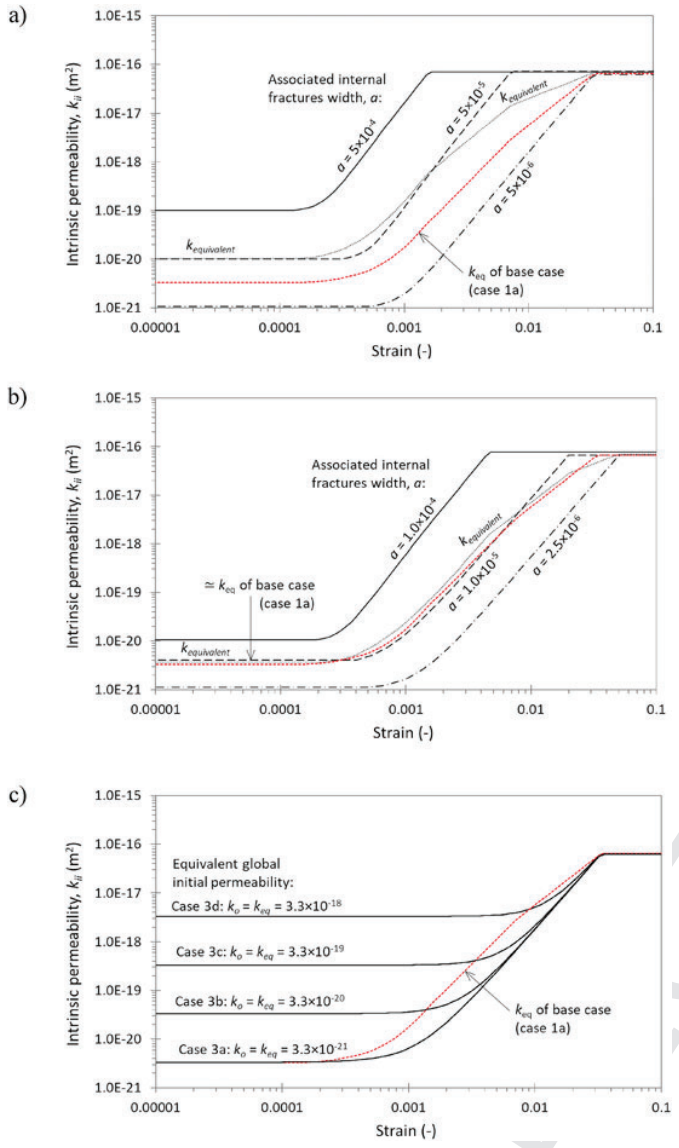

Fig. 11. Intrinsic permeability evolution for (a) Case 2a, (b) Case 2b, and (c) cases 3a-d).

magnitudes for the injection gas pressure and outflow are further from the measured data.

Fig. 14b presents the effect of initial permeability but with no changes in heterogeneity or the weighting distribution from the Base case. Case 5a and Case 5b assumes permeability values one half (C = 0.5) and double (C = 2) those of the Base case, respectively. The equivalent permeabilities of cases 5a and 5b are different from the Base case (see Table 3), but they are of the same order of magnitude. As expected, gas pressure, outflow and stress results with lower and higher permeabilities bracket the base case. The higher permeability (Case 5b) results in a better response at outflow both in terms of maximum magnitude and variation shape, but the pressure decay for both injection and array locations are less accurate than the Base case when compared with the measured data.

The effects of the maximum gas saturation assumption are assessed by Cases 6a ($S_{g,max}$ = 50%) and 6b ($S_{g,max}$ = 5%) and the results are shown in Fig. 14c. As before, higher or lower gas saturation values result in responses that bracket the Base case ($S_{g,max}$ = 30%), with the exception of the gas detected at array 2 during gas breakthrough (see Fig. S3a). A higher outflow is obtained with the lower gas saturation assumption and the radial stress decay yields a good agreement with measured data. However, gas pressure decay was not properly captured lying far from the measured response.

4.5. External system volumes

As indicted above, the volume factor allows, the use of more realistic injection system volume values. As it can be observed in Fig. 14d, the injection volume factor variation has a direct and significant effect on the gas pressure evolution and gas outflow, as well as on stress development. As expected, the smaller system injection volume involved (Case 7b), the faster the response in terms of gas pressure and stress showing more sudden variations and, in general, an earlier response as well. Also significantly more outflow is obtained. Alternatively, if more injection system volume is assumed (Case 7a), the gas outflow and generated gas pressure are lower as the system is able to accommodate more gas without affecting the material.

As shown in Fig. 3, the model incorporated the volumes connecting the 4 different radial cells at each array location. Different volume factors (F_a) have been assigned in cases 8a and 8b. As observed in Fig. 14e, with the values assumed, the volume factor in the arrays plays generally a minor role in the results obtained (and logically almost null effect concerning the injection gas pressure and stresses). The case with a higher volume factor at arrays (Case 8b) leads to a better delayed response in the gas pressure at arrays (see Fig. S5a) due to the gas absorbed by the arrays volume, however, with significantly less computed outflow.

4.6. Matrix n_{gas} power value

The effect of the gas matrix n-power variable (cases 9a and 9b) that defines the relative gas permeability of the material matrix (Eq. (3)) has been studied. It should be noted that the gas fracture n-power for the fractures was assumed to be fixed and equal to 1, as generally accepted for fractures[19] and the liquid n-power was also fixed to be 3, a common assumption for relative liquid permeability in low permeability materials [20,21].

Fig. 14f compares three cases to assess with different n-power. When the power is equal to 1 (Case 9a), matrix and fracture use the same relative permeability and less pressures and stresses are developed, despite a slightly larger computed outflow volume. In the other case (n_g = 3; Case 9b), significant less outflow volume and higher gas pressures are reached at both injection and array locations.

5. Spherical gas flow

A well validated model should be sufficiently general to be applied to other conditions. A spherical gas flow test performed in the same testing programme provides an opportunity to check the modelling approach and parameters developed for the axial gas flow test. Consequently, the same model and parameter values of the Base case (Case 1a) have been applied to the simulation of a spherical gas flow experiment and the results compared to the measured data **6**.

In the spherical gas flow test, the gas flow injection is performed at a point in the centre of the specimen. In the model, the internal injection at the centre of the sample is represented through a small volume with a single node connected to the sample and other free nodes applying the gas flow rate prescribed. The same modelling strategy, permeability heterogeneity, material properties, and equivalent injection system volume factor as in the Base case were adopted.

Results from spherical gas flow conditions are shown in Fig. 15, during the gas injection period from 735 to 835 days (as specified in the benchmarking exercise). The comparison with the experimental data show that the results exhibit a satisfactory agreement with observations properly capturing the history of injection gas pressure and the gas pressure decay. The measured outflow variation is also reasonably

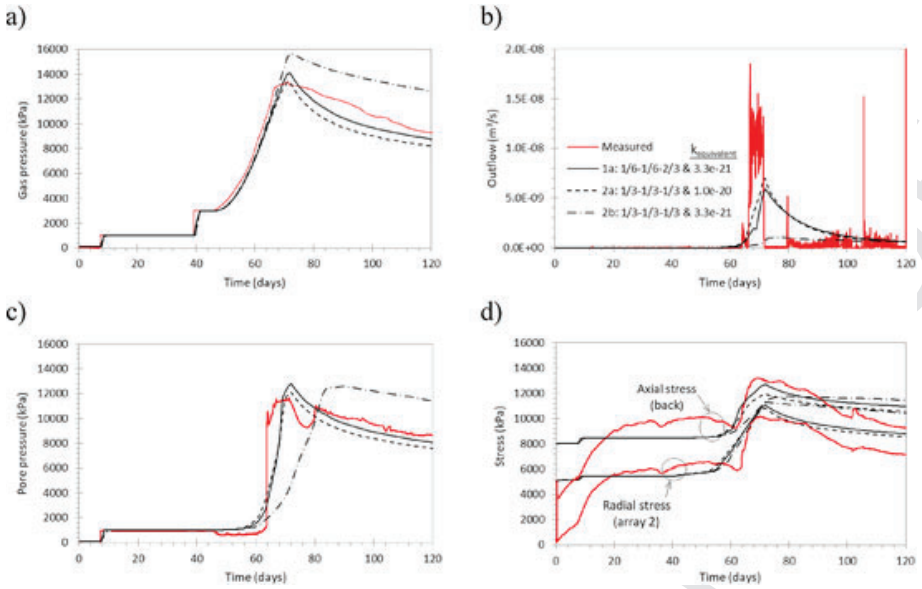

Fig. 12. Comparison between heterogeneity distribution weighting: (a) injection pressure, (b) outflow, (c) pore-pressure at array 2, and (d) axial and radial stresses (Cases 2).

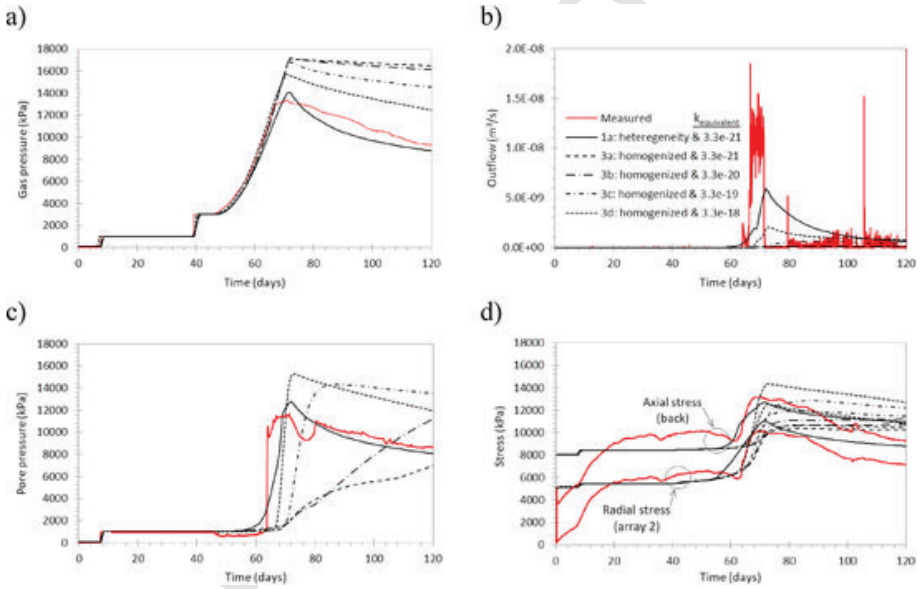

Fig. 13. Comparison between heterogeneity and homogeneity with different permeabilities: (a) injection pressure, (b) outflow, (c) pore-pressure at array 2, and (d) axial and radial stresses (Cases 3).

well captured although the computed outflow evolution is smooth in contrast with the oscillations recorded in the test. The variation of both radial and axial stresses is also well captured by the numerical model. To illustrate the development of the test according to the analysis, Fig. 16 shows the computed distributions of gas pressure gas flux obtained at various time of the gas injection process.

6. Concluding remarks

The proposed formulation has provided satisfactory simulations of axial and spherical gas flow through saturated Mx80 bentonite under constant volume boundary condition.

The formulation involves material heterogeneity and incorporates embedded fractures. An initial heterogeneity is introduced by means of a non-uniform distribution of parameters for permeability and retention curve. Intrinsic permeability has been considered with two terms, one corresponding to the matrix, and the other to embedded fractures. Matrix permeability varies according to Kozeny's law and the embedded fractures permeability varies according to a cubic law. A gas relative permeability function for each term is considered. Gas pressure-induced deformations during the test lead to variations of permeability due to changes in matrix porosity and, especially, fracture aperture.

Additional volumes have been introduced in the definition of the analysis domain in order to represent more closely the injection system and the measurement arrays. In accordance with the actual test procedure, a prescribed injection gas flow rate is the boundary condition applied and, hence, injection pressure is a calculated result.

A satisfactory reproduction of the axial gas flow test has been achieved. The analysis is able to capture gas breakthrough together with a good response in terms of peak and decay for both gas pressure and stresses evolution. Stress development is also well represented by the model. The variation of the computed outflow flow rate, however, is smooth whereas measurements exhibit irregular oscillations.

A comprehensive and systematic sensitivity program has been carried out for the axial flow test. The effect of the following model as-

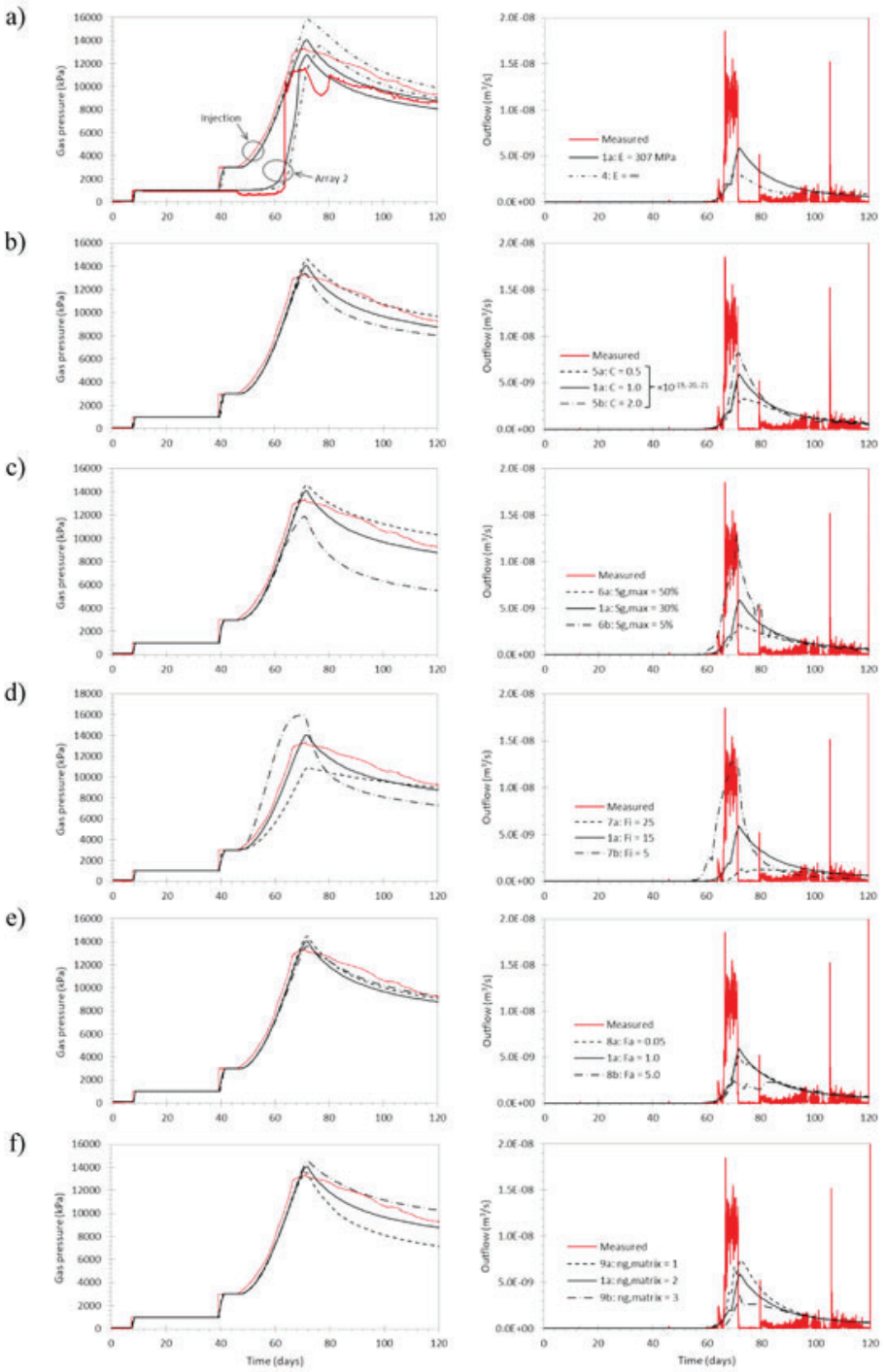

Fig. 14. Comparison results of gas pressure at injection (left), and outflow (right) for Base case 1a and (a) Case 4, (b) cases 5, (c) cases 6, (d) cases 7, (e) cases 8, and (f) cases 9 (Note: comparison results for pore pressure at arrays and axial/radial stresses from cases 5 to cases 9 are included in the Supplemental Material Figs. S2–S7).

pects and parameters have been explored and identified: heterogeneity and connectivity, intrinsic and relative permeability, stiffness, and additional volumes for the injection system and measurement arrays. Each sensitivity case produced a variety of results for the different sensors, improvements in a particular measurement was often accompanied by deterioration in the prediction of other sensor observations. The set of sensitivity calculations has contributed to a better understanding of the phenomenon and it has highlighted its high degree of complexity.

Modelling the spherical gas flow test using precisely the same assumptions and parameters calibrated in the axial gas flow test has resulted in a very good simulation of the experiment, suggesting that the developed formulation has a potentially wide range of applicability.

Declaration of competing interest

The authors declare that they have no known competing financial interests or personal relationships that could have appeared to influence the work reported in this paper.

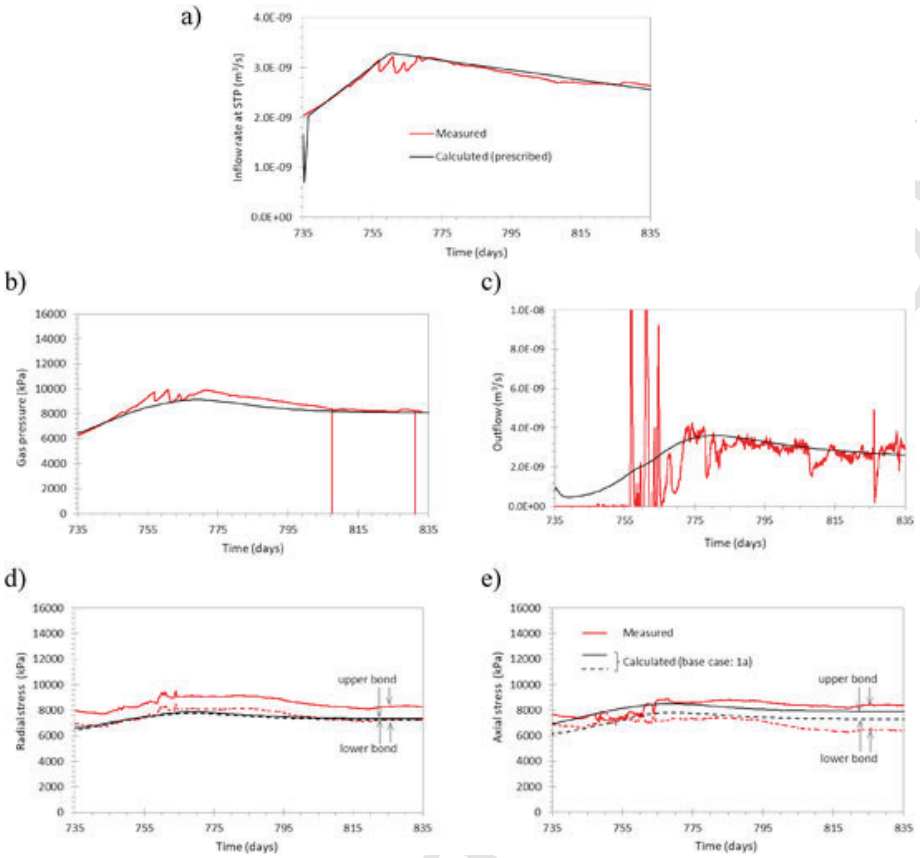

Fig. 15. Results from spherical gas flow and measurements: (a) inflow into the system, (b) injection pressure, (c) outflow, (d) axial stress and (e) axial stress.

Acknowledgments

The authors appreciate and thank Andra for funding this work, as well as all DECOVALEX-2019 Funding Organizations Andra, BGR/UFZ, CNSC, US DOE, ENSI, JAEA, IRSN, KAERI, NWMO, RWM, SÚRAO, SSM and Taipower for their financial and technical support of the work described in this report. The authors wish also to acknowledge the support of the International Centre for Numerical Methods in Engineering (CIMNE) and the funding received from the Spanish Ministry of Economy and Competitiveness through the "Severo Ochoa Programme for Centres of Excellence in R&D" (CEX2018-000797-S). The statements made in the report are, however, solely those of the authors and do not necessarily reflect those of the Funding Organizations.

Appendix A. Supplementary data

Supplementary data to this article can be found online at https://doi.org/10.1016/j.ijrmms.2020.104524.

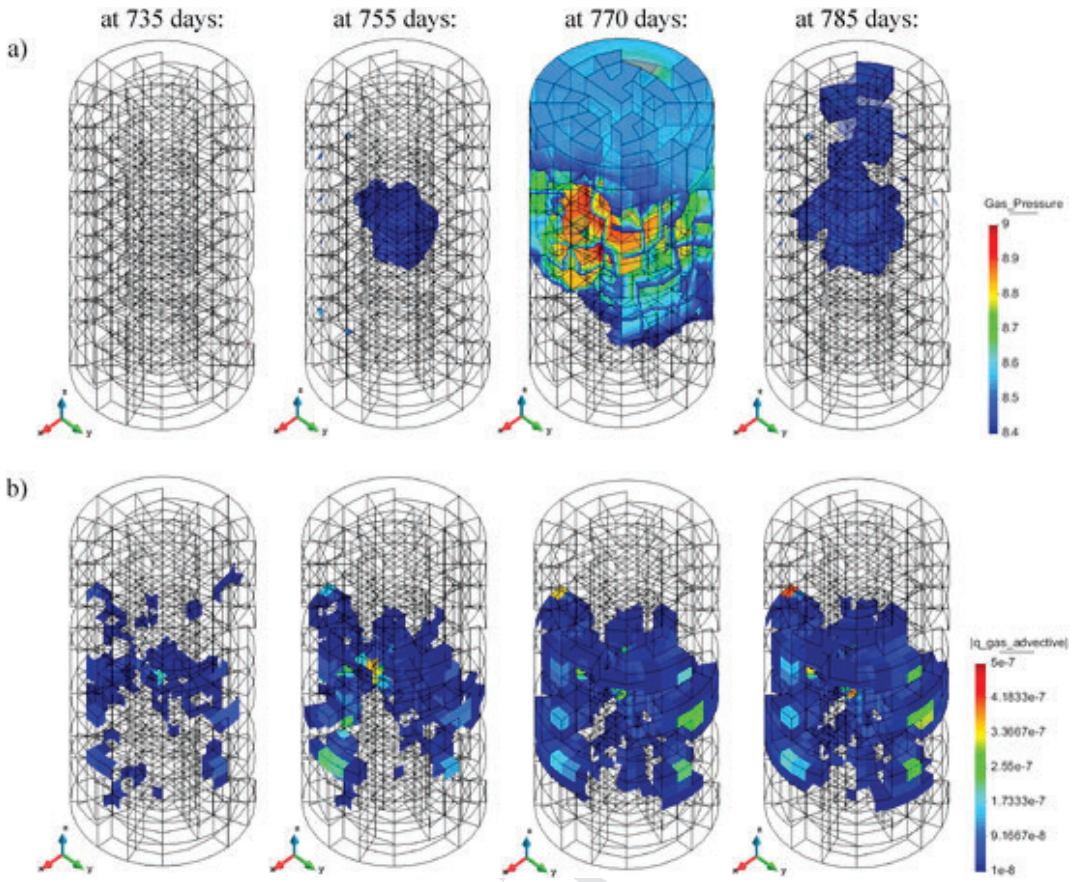

Fig. 16. (a) Gas pressure (in MPa) and (b) advective spherical gas flux (in m/s) results at 735, 755, 770, and 785 days.

References

1. J.F. Harrington, S.T. Horseman Gas transport properties of clays and mudrocks. Geol Soc. 1999;158:107–124. of London - Special Publications. doi:10.1144/GSL.SP.1999.158.01.09.
2. P. Marschall, T. Gimmi, S. Horseman Characterisation of Gas Transport Properties of the Opalinus Clay, a potential host rock formation for radioactive waste disposal. Oil Gas Sci Technol. 2005;60:121–139. doi:10.2516/ogst:2005008.
3. P.J. Binning, D. Postma, T.F. Russell, J.A. Wesselingh, P.F. Boulin Advective and diffusive contributions to reactive gas transport during pyrite oxidation in the unsaturated zone. Water Resour Res. 2007;43:1–12. doi:10.1029/2005WR004474.
4. D. Arnedo, E. Alonso, S. Olivella Gas flow in anisotropic claystone: modelling triaxial experiments. Int J Numer Anal Methods GeoMech. 2013;37(14):2239–2256. 0363-9061.
5. D. Arnedo, E. Alonso, S. Olivella, E. Romero Gas injection tests on sand/bentonite mixtures in the laboratory: experimental results and numerical modelling. Phys Chem Earth. 2008;33(1):237–247. doi:10.1016/j.pce.2008.10.061.
6. J.F. Harrington, C. Graham S, R.J. Cuss, S. Norris Gas network development in a precompacted bentonite experiment: evidence of generation and evolution. Appl Clay Sci. 2017;147:80–89. doi:10.1016/j.clay.2017.07.005.
7. A.C. Wiseall, R.J. Cuss, C.C. Graham, J.F. Harrington The visualization of flow paths in experimental studies of clay-rich materials. Mineral Mag. 2015;79:1335–1342. doi:10.1180/minmag.2015.079.06.09.
8. M. Mahjoub, A. Rouabhi, M. Tijani, J. Talandier Numerical study of callovo-oxfordian argillite expansion due to gas injection. Int J GeoMech. 2018;18:04017134. doi:10.1061/(ASCE)GM.1943-5622.0001050.
9. G. Guo, M. Fall Modelling of dilatancy-controlled gas flow in saturated bentonite with double porosity and double effective stress concepts. Eng Geol. 2018;243:253–271. doi:10.1016/j.enggeo.2018.07.002.
10. C. Zhu, Y. Li, Q. Zhao, et al. Experimental study and simulation of CO2 transfer processes in shale oil reservoir. Int J Coal Geol. 2018;191:24–36. doi:10.1016/j.coal.2018.03.002.
11. J.F. Harrington, R.J. Cuss, C. Graham S *Specification for DECOVALEX-2019: Task A: modEliNg Gas INjection ExpERiments (ENGINEER)*. Nottingham, UK: British Geological Survey Report Ref: BGS-DX-v3; 2016.
12. K.A. Daniels, J.F. Harrington The Response of Compact Bentonite during a 1D Gas Flow Test. British Geological Survey Open Report; 2017. Ref: OR/17/067.
13. E. Tamayo-Mas, J.F. Harrington, T. Brüning, et al. Modelling advective gas flow in compact bentonite: lessons learnt from different numerical approaches. Int J Rock Mech Min Sci. 2020. (this issue).
14. CODE_BRIGHT User's Guide Department of civil and environmental engineering (DECA), Barcelona school of civil engineering, Universitat Politècnica de Catalunya (UPC) and international center for numerical methods in engineering (CIMNE) https://deca.upc.edu/ca/el-departament/seccions/etcg/recerca/projectes/code_bright2020 https://www.gidhome.com/gid-plus/modules/modules-research/27/codebright/
15. S. Olivella, A. Gens, J. Carrera, E.E. Alonso Numerical formulation for a simulator (CODE-BRIGHT) for the coupled analysis of saline media. Eng Comput. 1996;13(7):87–112. doi:10.1108/02644409610151575.
16. S. Olivella, E.E. Alonso Gas flow through clay barriers. Geotechnique. 2008;58:157–168. doi:10.1680/geot.2008.58.3.157.
17. M.T. Van Genuchten A closed-form equation for predicting the hydraulic conductivity of unsaturated soils. SSSA (Soil Sci Soc Am) J. 1980;44(5):892–898. doi:10.2136/sssaj1980.03615995004400050002x.
18. E. Tamayo-Mas, J.F. Harrington, T. Brüning, et al. DECOVALEX-2019 Project: Task A - modElliNg Gas INjection ExpERiments (ENGINEER). Nottingham, UK: British Geological Survey. Ref: OR/18/049; 2018.
19. H. Ramajo, S. Olivella, J. Carrera, X. Sánchez-Vila Simulation of gas dipole tests in fractures at the intermediate scale using a new upscaling method. Trans Por Med. 2002;46:269–284. doi:10.1023/A:1015083122787.
20. A. Gens, M. Sanchez, L.D.N. Guimaraes, et al. A full-scale in situ heating test for high-level nuclear waste disposal: observations, analysis and interpretation. Geotechnique. 2009;59(4):377–399. doi:10.1680/geot.2009.59.4.377.
21. A. Rodriguez-Dono, S. Olivella, N. Mokni Assessment of a high-level spent nuclear fuel disposal model. Env Geotech. 2020;7(1):42–58. doi:10.1680/jenge.18.00017.